Journal of Controlled Release 351 (2022) 834–846

Contents lists available at ScienceDirect

Journal of Controlled Release

journal homepage: www.elsevier.com/locate/jconrel

R11 modified tumor cell membrane nanovesicle-camouflaged nanoparticles with enhanced targeting and mucus-penetrating efficiency for intravesical chemotherapy for bladder cancer

Bin Zheng [a,1], Zhenghong Liu [a,1], Heng Wang [a,1], Li Sun [a], Wing-Fu Lai [a,f], Haibao Zhang [b], Jinxue Wang [c], Yang Liu [d], Xiaowen Qin [a], Xiaolong Qi [a], Shuai Wang [a], Youqing Shen [e,**], Pu Zhang [a,*], Dahong Zhang [a,*]

[a] Urology & Nephrology Center, Department of Urology, Zhejiang Provincial People's Hospital, Affiliated People's Hospital, Hangzhou Medical College, Hangzhou, Zhejiang 310014, China
[b] Oncology Research Lab, Key Laboratory of Environment and Genes Related to Diseases, Ministry of Education, Xi'an Jiaotong University, Xi An Shanxi 710049, China
[c] Rehabilitation Medcine Center, Department of Neuroelectrophysiology, Zhejiang Provincial People's Hospital, Affiliated People's Hospital, Hangzhou Medical College, Hangzhou, Zhejiang 310014, China
[d] Cancer Center, Department of Ultrasound Medicine, Zhejiang Provincial People's Hospital, Affiliated People's Hospital, Hangzhou Medical College, Hangzhou, Zhejiang 310014, China
[e] Center for Bionanoengineering and Key Laboratory of Biomass Chemical Engineering of Ministry of Education, College of Chemical and Biological Engineering, Zhejiang University, Hangzhou, Zhejiang 310014, China
[f] Department of Applied Biology and Chemical Technology, Hong Kong Polytechnic University, HongKong, China

ARTICLE INFO

Keywords:
Bladder cancer
Intravesical therapy
Cell membrane-camouflaged nanoparticle
Mucus-penetrating

ABSTRACT

Intravesical chemotherapy is generally used in the clinic for treating bladder cancer (BCa), but its efficacy is limited due to the permeation barrier and side effects caused by the off-targeting of normal urothelial cells. In this study, BCa cell-derived membrane nanovesicles were used as drug carriers, and their homologous tumor-targeting capacity was utilized. A BCa-targeting hendeca-arginine peptide was functionalized onto the nanovesicles to impart a mucus-penetrating ability and thus overcome the permeation barrier. The tumor-targeting and mucus-penetrating nanovesicles were stable in urine, were highly permeable to the glycosaminoglycan layer, and specifically targeted BCa. The vesicles were internalized through caveolin-mediated endocytosis, were transported to nonlysosome-localized intracellular regions, and efficiently infiltrated bladder tumor spheroids. In *in vivo* intravesical chemotherapy, the nanovesicles achieved chemo-resection in murine orthotopic BCa models. This BCa-targeting and mucus-penetrating drug delivery system may be promising for the intravesical chemotherapy of BCa.

1. Introduction

Bladder cancer (BCa) is among the most prevalent cancers worldwide. Additionally, BCa has the highest cost of all types of cancer for lifelong follow-up and frequent treatment [1,2]. The standard recommended treatment for nonmuscle invasive BCa is to perform a transurethral resection of bladder tumors followed by intravesical therapy [3,4]. Adjuvant intravesical therapy is used to kill residual tumor cells, but the risk of recurrence is reduced by <5% [5–7].

Due to the unique structure of the bladder, systemic delivery of drugs may be difficult to distribute to the bladder site, and intravesical therapy is a common route of administration for clinical treatment of BCa [8]. however, the luminal protective barrier, which mainly comprises a glycosaminoglycan (GAG) layer, together with densely packed BCa

* Corresponding authors at: Urology & Nephrology Center, Department of Urology, Zhejiang Provincial People's Hospital, Affiliated People's Hospital, Hangzhou Medical College, Hangzhou, Zhejiang 310014, China.
** Corresponding author at: Center for Bionanoengineering and Key Laboratory of Biomass Chemical Engineering of Ministry of Education, College of Chemical and Biological Engineering, Zhejiang University, Hangzhou, Zhejiang 310014, China.
E-mail addresses: shenyq@zju.edu.cn (Y. Shen), zhangpuxjtuer@163.com (P. Zhang), urology@zju.edu.cn (D. Zhang).
[1] These authors contributed equally to this work.

https://doi.org/10.1016/j.jconrel.2022.09.055
Received 2 July 2022; Received in revised form 21 September 2022; Accepted 26 September 2022
Available online 10 October 2022

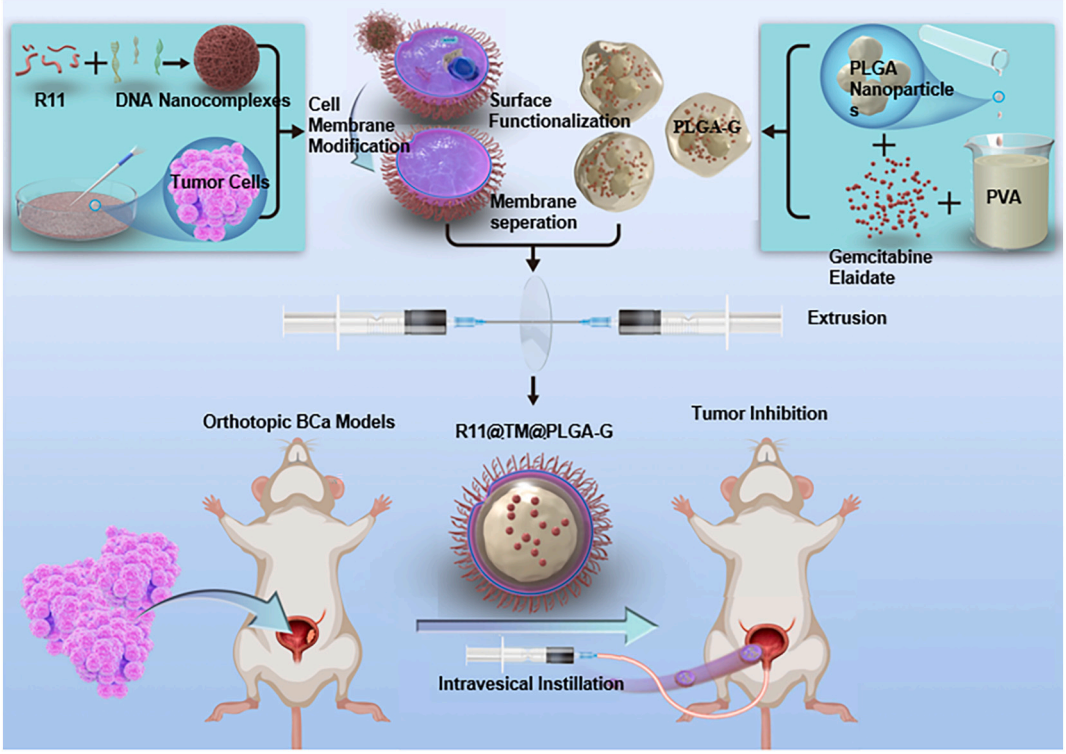

Fig. 1. Hendeca-arginine peptide (R11) was polymerized with DNA to form nanocomplexes, which enabled one-step surface-functionalization of tumor cell membrane with large amounts of R11 at the extracellular side of cell membrane. The tumor cell membrane fragments with the R11 shell were used to encapsule gemcitabine-loaded PLGA nanoparticles by extrusion to construct a dual-targeting and mucus-penetrating drug delivery system for intravesical chemotherapy in bladder cancer.

tissue, serves as an obstacle to drug penetration during intravesical therapy [9–11]. A variety of mucus-penetrating nanoparticles have been used to transport drugs to tumor regions [12–16], but when the nanoparticles were applied for practical use in orthotopic BCa models, the outcomes were far below expectations [17]. Another issue is that off-targeting occurs with normal urothelial cells, which leads to higher risks of side effects.

Inspired by the high biocompatibility and homologous tumor-targeting properties of tumor cell membrane-camouflaged nanoparticles [18], we shielded gemcitabine-loaded PLGA nanoparticles (PLGA-G) into BCa cell-derived membrane-camouflaged nanoparticles (TM) to construct a drug delivery system for intravesical instillation. [17,19] However, TM is not permeable to the negatively charged GAG layer. Because hendeca-arginine peptide (R11) is positively charged and targets tumor in BCa, the peptide was used for surface functionalization of TM to achieve a dual targeting and mucus-penetrating capacity. Compared with directly modifying TM with R11, modifying membranes of live cells before the membrane is isolated has several advantages [20]; for example, it is convenient to separate TM with unattached R11, and the correct positioning of R11 remains at the extracellular side of the membrane. The previous methods used for cell membrane functionalization usually require two or more synthesis or modification steps [21]. In this study, nanocomplexes generated by simply mixing R11 with random-sequence DNA were coincubated with BCa cells to functionalize R11 onto the cell membrane through electrostatic interactions with phospholipids. Compared to surface functionalization with free R11, surface functionalization with nanocomplexes greatly increased the amount of R11 that remained on the cell membrane. BCa cells coated with R11 shells were then transferred for extrusion to synthesize R11-functionalized TM (R11@TM). The surface modification approach was cell-friendly and convenient to conduct. The intravesical drug delivery system comprising R11@TM-camouflaged PLGA-G (R11@TM@PLGA-G) exhibited excellent BCa-targeting capacity and mucus-penetrating efficiency and even chemo-resected most tumors in murine orthotopic BCa models (Fig. 1). Thus, R11@TM@PLGA-G offers translational advantages and warrants further development as a therapeutically potent strategy for BCa intravesical chemotherapy.

2. Material and methods

2.1. Materials

R11 was purchased from GL Biochem., Ltd. (Shanghai, China). DNA was purchased from Tsingke Biotechnology Co., Ltd. (Beijing, China). Ethylacetate, PLGA and PVA were purchased from Macklin Biochemical Co., Ltd. (Shanghai, China). Gemcitabine elaidate was purchased from MedChemExpress. Cell trackers such as Dil and Dio were purchased from Beyotime Institute of Biotechnology (Shanghai, China). Coumarin-6 was purchased from Sigma (Shanghai, China). Endoplasmic reticulum (ER) tracker, Golgi tracker, and LysoTracker were purchased from Beyotime Institute of Biotechnology. (Shanghai, China). Chlorpromazine, filipin, and ethyl isopropyl amiloride (EIPA) were purchased from Macklin Biochemical Co., Ltd. (Shanghai, China). Artificial urine and coumarin-6 were purchased from Solarbio Life Science Co., Ltd. (Beijing, China). 4,6-Diamino-2-phenylindole (DAPI) was purchased from Yeasen Biotech Co., Ltd. (Shanghai, China). DMEM (high glucose), penicillin–streptomycin, trypsin-EDTA, fetal bovine serum (FBS), and phosphate-buffered saline (PBS, pH 7.4) were obtained from Thermo Fisher Scientific (Waltham, MA, USA). Cell Counting Kit-8 (CCK-8) was purchased from Yeasen Biotech Co., Ltd. (Shanghai, China). Isoflurane was purchased from RWD Life Science Co., Ltd. (Shenzhen, China).

2.2. Cell membrane fragments extraction

Solutions containing nanocomplexes were prepared by mixing one volume of an R11 solution with an equal volume of a DNA(5'-

ATCAACCTTGGTTATACGATGACCGGTGCG-3′) solution at different NP ratios (5, 10 or 20). The generated nanocomplexes were designated NP5, NP10, and NP20. During nanocomplex preparation, the DNA solution was dropwise added into the R11 solution under vigorous stirring as previously described [22]. T24 cells were incubated with nanocomplexes at a concentration of 2 μM R11 for 12 h. T24 cells were then washed twice with PBS to remove unattached nanocomplexes. T24 cells were harvested by scraping. Cell membranes were separated from parental cells by resuspending T24 cells in hypotonic buffer, then the mixture was centrifuged at 700 ×*g* for 10 min at 4 °C. Cell membranes were obtained by centrifuging the supernatant at 14,000 x g for 30 min at 4 °C [23]. Cell membrane fragments without R11 shells were prepared by the same method. Cell membrane fragments without R11 shells were prepared by the same method.

2.3. PLGA-G preparation

PLGA-G was prepared using the solvent evaporation method. Ten milligrams of PLGA and 1 mg of gemcitabine elaidate (G) were dissolved in an organic solvent (ethyl acetate). The mixture was added dropwise into ultrapure water with vigorous stirring. Then, the mixture above was added dropwise into a PVA solution followed by sonication. The volatile organic solvent was removed by evaporation. The drug loading content (DLC) and drug loading efficiency (DLE) of PLGA-G were calculated according to the following equations: DLC (%) = $W_{(\text{drug in PLGA-G})}$/ $W_{(\text{drug-loaded PLGA-G})}$ × 100%; DLE (%) = $W_{(\text{drug in PLGA-G})}$/ $W_{(\text{total feeding drug})}$ × 100%.

2.4. TM@PLGA-G and R11@TM@PLGA-G preparation

To encapsulate PLGA-G into nanovesicles generated from T24 cell membrane fragments, PLGA-G (1 ml, 1 mg/ml) was added dropwise to TM or R11@TM (0.5 mL, 0.3 mg/ml) under vigorous stirring. The above mixture was transferred to a micro extruder (Avanti Polar Lipids) with a 400 nm polycarbonate membrane insert. After repeated cycles of extrusion, the product was centrifuged at high speed and rinsed with sterilized ultrapure water to obtain TM@PLGA-G or R11@TM@PLGA-G.

2.5. ELISA determination of R11 immobilized on the outer surface of cell membrane vesicles

The detection method of R11 located at the outer surfaces of the nanoparticles was based on a modified ELISA analysis, which was used for detecting L-arginine. The standard curve was generated by using R11 or NP5 nanocomplexes as standards. Relating to samples in all NP5 nanocomplex-treated groups, the minimum or maximized amount of R11 located at the outer surface of nanoparticles was calculated according to two different standard curves. To block the transfer of noncovalently bounded R11 from intracellular components to membrane fragments, the heparin at the concentration being 25 μg/ml was coincubated with cell lysates. For the group named as coincubation with cell lysates, NP5 nanocomplexes at the concentration of R11 being 2 μM were coincubated with cell lysates for 12 h.

2.6. In vitro release of gemcitabine

The release efficiency of G in different formulations was determined in PBS (pH = 7.4) or DMEM at 37 °C. Two milliliters of PLGA-G, TM@PLGA-G or R11@TM@PLGA-G with a concentration of G of 1 mg/ml was added to dialysis bags (cutoff molecular weight: 3500 Da). The dialysis bag was immersed in PBS buffer or urine with shaking (70 rpm/min) at 37 °C. At designated intervals, 1 ml of dialysis buffer was transferred for HPLC analysis. Each data point was tested in triplicate in three independent experiments. The kinetics of drug release from the nanoparticles was determined by fitting into zero-order release kinetics, first-order release kinetics, and Higuchi kinetics. Kinetic analysis was performed also on the release profiles *via* the Korsmeyer–Peppas kinetics to study the release mechanism.

2.7. Cell culture

BCa cells (T24, T24l, and 253 J) and normal urothelium cells (SVHUC-1) were cultured in DMEM. All cell lines were supplemented with 10% fetal bovine serum and 100 U/mL 1% penicillin/streptomycin and maintained at 37 °C. T24, 253 J, and SVHUC-1 cells were obtained from the National Collection of Authenticated Cell Cultures, China.

2.8. BCa targeting efficiency

SVHUC-1, T24, T24l and 253 J cells were separately seeded into laser confocal Petri dishes (1.0 × 10ˆ5 cells per microplate). After incubation for 12 h, R11@TM labeled by Dil or TM labeled by Dil was incubated with SVHUC-1, T24, T24l or 253 J for 4 h. The Cells were washed with precooled PBS three times, fixed with 4% formalin and stained with DAPI. Confocal laser scanning microscopy (CLSM) (Leika TCS SP5 Confocal, LEIKA Inc., California, US) was used to observe the BCa targeting efficiency. ImageJ software was used for analysis.

2.9. Endocytosis dynamics

The T24 cells were seeded into laser confocal Petri dishes (1.0 × 10ˆ5 cells per microplate) and incubated for 12 h. Then , the T24 cells were incubated with R11@TM labeled by Dil for different times. The cells were washed with precooled PBS three times, fixed with 4% formalin and stained with DAPI. The samples were transferred for CLSM observation. ImageJ software was used for analysis.

2.10. Intracellular colocalization of dual components of R11@TM

T24, T24l and 253 J cells were separately seeded into laser confocal Petri dishes (10^5 cells per microplate) and incubated for 12 h. R11 was labeled with TARMA at its N-terminus, and cell membrane nanovesicles were stained with Dio. Dual-labeled R11@TM was incubated with T24, T24l and 253 J for 4 h. The cells were washed with precooled PBS three times and transferred for CLSM observation. ImageJ software was used for analysis.

2.11. Endocytosis pathway determination

The T24, T24l and 253 J cells were separately seeded into laser confocal Petri dishes (10^5 cells per microplate) and incubated for 12 h. Endocytosis inhibitors (filipin, 1 μg/ml; chlorpromazine hydrochloride (CPZ), 10 μg/mL; ethyl isopropyl amiloride (EIPA), 10 μg/mL) were separately incubated with the cell lines above for 1 h to inhibit their correlated endocytosis pathways. Incubation at 4 °C was performed to block energy-dependent endocytosis. Fluorescently labeled R11@TM (0.3 mg/ml) was incubated for another 2 h with cells that were pretreated with endocytosis inhibitors or at 4 °C. Cells were washed with precooled PBS three times, fixed with 4% formalin and stained with DAPI. The samples were transferred for CLSM observation. ImageJ software was used for analysis.

2.12. Subcellular distribution of R11@TM

T24, T24l and 253 J cells were separately seeded into laser confocal Petri dishes (10^5 cells per microplate) and incubated for 12 h. The Dil-labeled R11@TM was incubated with cells for 4 h. ER tracker, Golgi tracker, and LysoTracker were separately used to stain organelles with green fluorescence. The samples were transferred for CLSM observation. ImageJ software was used for the colocalization analysis.

2.13. In vitro cytotoxicity assay

T24 cells were seeded into 96-well plates (5000 cells per well) and incubated for 12 h. G, PLGA-G, TM@PLGA-G and R11@TM@PLGA-G were separately incubated with T24 cells at concentrations of 0.5–20.0 μg/ml for 24 h and 48 h. After that, the medium in each well was replaced with 0.2 ml of fresh medium containing a 10% CCK-8 solution for another 2 h. The absorbance in each well was measured at 450 nm using a microplate spectrophotometer. Each data point was tested in triplicate in three independent experiments.

2.14. Wound-healing assay

T24 cells were seeded in 6-well plates (8×10^5 cells per well) and incubated for 24 h. Once the influence of the cells reached 100%, confluent T24 monolayers were scraped with a 200 μl pipette tip to create a scratch wound. Nonadherent cells were washed away, and the remaining cells were then incubated with the indicated treatment. The wound healing areas were observed at 0 h and 24 h. The cell migration distance was calculated by subtracting the wound width at 0 h from the wound width at 48 h.

2.15. Transwell assay

T24 cells were incubated with the indicated treatments, and then T24 cells at a density of 5×10^5 cells per well were seeded into the upper chambers of Transwell plates with 8.0 μm pore polyester membrane inserts (Corning, Thermo Fisher Scientific Inc., Waltham, US), whereas the bottom chambers were filled with complete cell culture media. The cells were grown for 24 h. The cells on the top of the filter were removed, and the cells on the underside of the top chamber were fixed with 4% formalin and stained with 0.1% crystal violet for 10 min at room temperature. The cell numbers were counted under an inverted microscope (TS 100, NIikon Ti, Japan).

2.16. GAG permeation assay

A chondroitin sulfate solution was used to cover the topside of a polyester membrane filter (0.4 μm pore size) with a density of 0.18 mg/cm^2. G was replaced with coumarin-6 to fluorescently label PLGA-G, TM@PLGA-G and R11@TM@PLGA-G. Then, 20 μl of the above drugs was separately added to the upper chamber at a concentration of 4 mg/ml coumarin-6, and 1 ml of PBS buffer was added to the lower chamber. At different time points, 100 μl of PBS buffer containing the leakage from the upper chamber was transferred for fluorescence intensity analysis. A Multi-Mode Microplate Reader (Synergy Mx, Bio-Tek Instruments Inc., Winooski, US) was used to measure the fluorescence intensity with excitation at 337 nm and emission at 560 nm. Concentrations were calculated according to a standard curve. Each data point was tested in triplicate in three independent experiments.

2.17. Penetration efficiency in tumor spheroids

T24 cells were suspended in DMEM (containing 0.12% *w/v* methylcellulose) at a density of 1×10^6 cells per ml. Then, 25 μl of the cell suspension was dropped on the lid of the cell culture plate to form uniform droplets. Ten milliliters of PBS was added to the plate to keep the droplets moist. After 72 h, dense spheroids were transferred to a low adhesion 96-well plate with one spheroid per well and incubated for another 72 h. G was replaced with coumarin-6 to fluorescently label PLGA-G, TM@PLGA-G and R11@TM@PLGA-G and filipin-pretreated R11@TM@PLGA-G. The drugs above with a concentration of 2 mg/ml coumarin-6 were separately incubated with T24 spheroids for 4 h. T24 spheroids were washed twice with PBS and imaged by CLSM. ImageJ software was used for analysis.

2.18. Targeting and penetration efficiency in murine orthotopic BCa models

All animal procedures were approved by the Laboratory Animal Management Committee at Zhejiang Provincial People's Hospital (20220022). All animal procedures were performed according to the guidelines of the Administration Committee of Experimental Animals in Zhejiang Province and the Ethics Committee of Zhejiang Provincial People's Hospital. Six- to eight-week-old nu/nu female mice were anesthetized by inhalation of 1% isoflurane in an oxygen gas mixture and kept on a heated platform during catheterization procedures. Lubricated angiocatheters were inserted into the urethra. After full insertion, the bladder was flushed with 80 μl of sterile PBS and pretreated with 80 μl of poly-L-lysine for 15 min. A single-cell suspension of 5×10^5 GFP-transfected T24 cells in 100 μl of PBS was inoculated into the bladder and preserved for 1 h. During the entire procedure, the mice were kept under anesthesia for 2 h before the catheter was gently removed from the urethra. The mice were monitored every day for any signs of pain and distress. The nu/nu female mice bearing BCa were anesthetized by inhalation of 1–2% isoflurane in an oxygen gas mixture and kept on a heated platform during catheterization procedures. Lubricated angiocatheters were inserted into the urethra. After full insertion, the bladder was flushed with 80 μL of sterile PBS. TM and R11@TM were both labeled with Dil. Then, 100 μl of TM and R11@TM (0.3 mg/ml) were intravesically instilled and preserved for 2 h, respectively. The bladder was washed twice with PBS. The mice were sacrificed immediately. The bladders were harvested, frozen and sectioned (20 μm thick) in a cryostat. The sections were examined by using CLSM. ImageJ software was used for analysis.

2.19. Intravesical therapy in murine orthotopic BCa models

The nu/nu female mice bearing BCa originating from luciferase-transfected T24 cells were obtained as shown in 2.17. They were anesthetized by inhalation of 1–2% isoflurane in an oxygen gas mixture and kept on a heated platform during catheterization procedures. Lubricated angiocatheters were inserted into the urethra. After full insertion, the bladder was flushed with 80 μl of sterile PBS. G, PLGA-G, TM@PLGA-G and R11@TM@PLGA-G with a dose of 10 mg/kg G were intravesically instilled and preserved for 2 h. Saline was also intravesically instilled as in the control group. Intravesical instillation was performed every five days for a total of five times. The mice were weighed every 2 d. The mice were intraperitoneally injected with 100 mg/kg D-luciferin to monitor the *in vivo* bioluminescence of tumors using the IVIS Spectrum system (IVIS Lumina XRMS Series III (PerkinElmer), PerkinElmer Inc., Waltham, US) every 5 d. The mice were sacrificed one day after the final step of intravesical instillation, and the tissues (including bladder, heart, liver, spleen, lung and kidney) were harvested for further histopathological examination by HE staining. The tissues were imaged by an inverted microscope (TS 100, NIikon Ti, Japan).

2.20. Statistical analysis

Data are expressed as the means ± standard deviation (SD). Significant differences were determined using Student's *t*-test or one-way ANOVA as appropriate. A 2-tailed $p < 0.05$ was considered to be statistically significant. *$p < 0.05$; **$p < 0.01$; ***$p < 0.001$; ****$p < 0.0001$. All data were analyzed with GraphPad Prism Version 8.0 (GraphPad Software, CA, USA.)

3. Results and discussion

3.1. Physicochemical properties

The surface functionalization of TM with R11 was conducted by modifying membranes of live cells with R11 before membrane isolation.

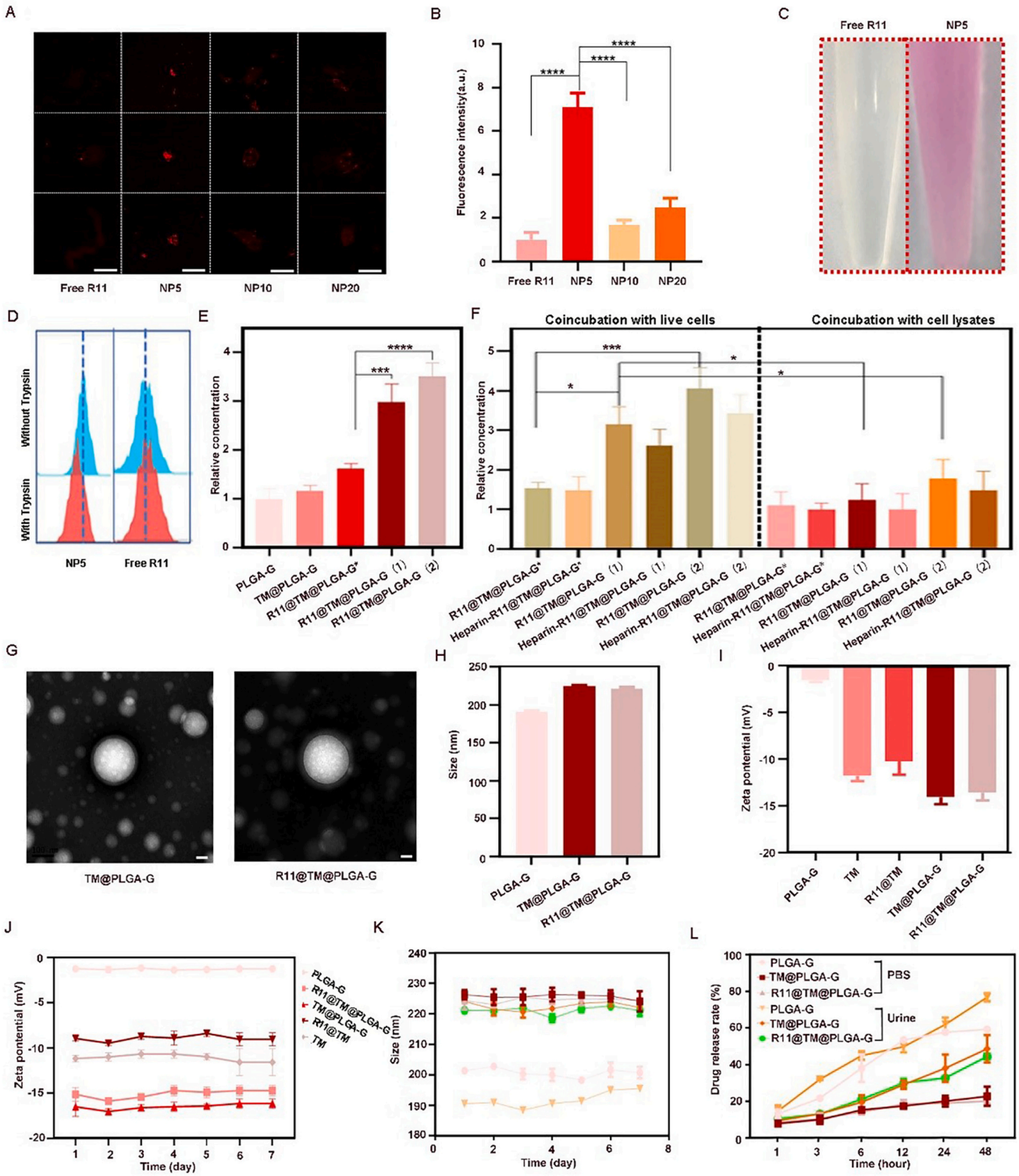

Fig. 2. Physicochemical properties. A) CLSM images of R11 deposited onto the cell membrane fragments in groups treated with nanocomplexes at different NP ratios; scale bar: 50 μm. B) Statistical analysis of different treatments in A); **** $p < 0.0001$. C) Images of cell membrane fragments with R11 shells in groups treated with free R11 or NP5 nanocomplexes. D) Flow cytometry analysis of detachment of R11 from cell membrane fragments by trypsin digestion. E) The ELISA analysis of R11 located at the outer surface of nanoparticles; *: R11@TM@PLGA-G of free-R11-treated group; (1) or (2): The minimum amount or maximized amount in R11@TM@PLGA-G of NP5-nanocomplex-treated group. F): The ELISA analysis of R11 located at the outer surface of nanoparticles; *: R11@TM@PLGA-G of free-R11-treated group; (1) or (2): The minimum amount or maximized amount in R11@TM@PLGA-G of NP5-nanocomplex-treated group. G) Transmission electron microscope images of TM@PLGA-G and R11@TM@PLGA-G; Scar bar: 25 nm. H) The average particle size of PLGA-G, TM@PLGA-G and R11@TM@PLGA-G. I) The average zeta potential of PLGA-G, TM, R11@TM, TM@PLGA-G and R11@TM@PLGA-G. J) The stability of the Zeta potential of PLGA-G, TM@PLGA-G and R11@TM@PLGA-G. K) The stability of the size of PLGA-G, TM@PLGA-G and R11@TM@PLGA-G. l) Drug release of PLGA-G, TM@PLGA-G and R11@TM@PLGA-G. *** $p < 0.001$、**** $p < 0.0001$.

Table 1
Release kinetic parameters of PLGA-G, TM@PLGA-G and R11@TM@PLGA-G.

	PLGA-G	TM@PLGA-G	R11@TM@PLGA-G
k0	1.924	1.176	1.080
r^2	−0.366	0.353	0.057
k1	0.051	0.017	0.015
r^2	0.490	0.600	0.347
kH	12.149	7.187	6.712
r^2	0.801	0.949	0.899
kKP	20.942	8.989	10.021
n	0.330	0.431	0.376
r^2	0.968	0.974	0.969

At a concentration of 2 μM, R11 was internalized by live cells through fast transduction (Fig. S1A), a small amount of R11 remained at the surface of the cell membrane. When R11 was polymerized with DNA to form nanocomplexes, R11 aggregated on the cell membrane, which was followed by endocytosis (Fig. S1B); thus, high amounts of R11 were deposited on the surface of the cell membrane. For the nanocomplexes, different ratios of nitrogen to phosphorus (NP) regulated the loaded amount of R11 at the cell membrane, and NP5 nanocomplexes achieved the maximum ratio. As suggested in Fig. 2A-B, the fluorescence intensity per 25 μm^2 of cell membrane fragments was 8.5 ± 2.9-fold higher in the NP5 nanocomplex-treated group than in the free R11-treated group. The difference in the loaded amount between the NP5 assembly-treated group and the free R11-treated group was visible even to the naked eye (Fig. 2C). Trypsin digestion reduced the total loaded amount of R11 in the NP5 nanocomplex-treated group but not in the free R11-treated group, indicating that the polymerization of R11 and DNA at an NP ratio of five improved the retention amount of R11 on the cell membrane and that R11 was located on the extracellular side of the membrane (Fig. 2D). After repeated cycles of extrusion, R11 shells remained right-side-out in both the NP5 nanocomplex-treated group and the free R11-treated group (Fig. 2E). Incubation of heparin with cell lysates should block the transfer of non-covalently bounded R11 from intracellular components to membrane fragments. [[22] [24],] The binding affinity of nanoparticles for antibodies against L-arginine did not decrease in those heparin-treated groups compared to the heparin-untreated groups (Fig. 2F). Furthermore, nanoparticles generated by our surface functionalization method had higher binding affinities with antibodies against L-arginine compared with nanoparticles generated by mixing cell lysates with R11 or NP5 nanocomplexes (Fig. 2F). Therefore, the endocytosis of NP5 nanocomplexes strengthened R11's attachment to the outer surface of cell membrane fragments. And as indicated in **Fig. S2**, the procedure of extrusion could not exfoliate cell membrane-immobilized R11 component. Western blotting analysis of cell membrane-specific protein markers indicated pan-cadherin, Epidermal Growth Factor Receptor(EGFR) and Na +/K + -ATPase remained at the surface of TM and R11@TM (**Fig. S3**). Overall, the whole procedure of surface functionalization with R11 involved only one-step incubation without introducing any exogenous crosslinkers into the culture medium. Therefore, the surface functionalization approach in our study is cell-friendly and simple to conduct.

TEM analysis indicated that both TM and R11@TM could encapsulate PLGA-G to form monodisperse spherical nanoparticles (Fig. 2G). Because of the complex environment in urine, it is usually hypotonic and acidic. So we put the nanovesicles into artificial urine to test their stability [11,25]. The DLS analysis showed that the average particle sizes of PLGA-G, TM@PLGA-G and R11@TM@PLGA-G were 190.6 ± 0.5 nm, 224.1 ± 0.5 nm and 221.1 ± 0.9 nm (Fig. 2H), respectively. The zeta potentials of PLGA-G, TM, R11@TM, TM@PLGA-G and R11@TM@PLGA-G were − 1.2 ± 0.14, −15.1 ± 0.6, −16.5 ± 0.9, −8.9 ± 0.2, −11.1 ± 0.3 respectively (Fig. 2I). The encapsulation efficiency of G in PLGA nanoparticles was calculated to be 93%, and the drug loading rate was 16.8%. The stability of R11@TM@PLGA-G in PBS (pH = 7.4) and in artificial urine (pH = 6.5) was measured by the DLS analysis and the zeta potential analysis. As shown in Fig. 2J-K, the average diameter and the zeta potential of R11@TM@PLGA-G remained almost the same during seven days of incubation in PBS (pH = 7.4) and artificial urine. The G release kinetics of all formulations were also investigated in PBS and in artificial urine. Compared with PLGA-G and TM@PLGA-G, the amount of G released in the R11@TM@PLGA-G group was significantly reduced at all points of incubation time (Fig. 2L). The release profiles of all of the tested nanoparticles (PLGA-G, TM@PLGA-G and R11@TM@PLGA-G) in urine follow most closely the Higuchi kinetics (Table 1), which depicts the release of drug molecules from an insoluble matrix as a square root of time-dependent process based on the Fickian diffusion. The process of drug release from our nanoparticles is therefore expected to involve the penetration of the release medium into the polymer matrix and the diffusion of the drug molecules from the matrix to the external release medium. The n values obtained by fitting the release profiles of different nanoparticles into the Korsmeyer-Peppas kinetics, which describes the log fraction of drug release with respect to log time, are in the range from 0.330 to 0.431, showing that drug release from our nanoparticles follows the mechanism of Fickian diffusion. Incorporation of TM and R11 onto PLGA-G nanoparticles appears to have no impact on the drug release kinetics and drug release mechanism shown by the PLGA-G nanoparticles. Taking all these findings into consideration, the surface functionalization of R11 inhibited the undesired release of G from R11@TM@PLGA-G in the harsh environment.

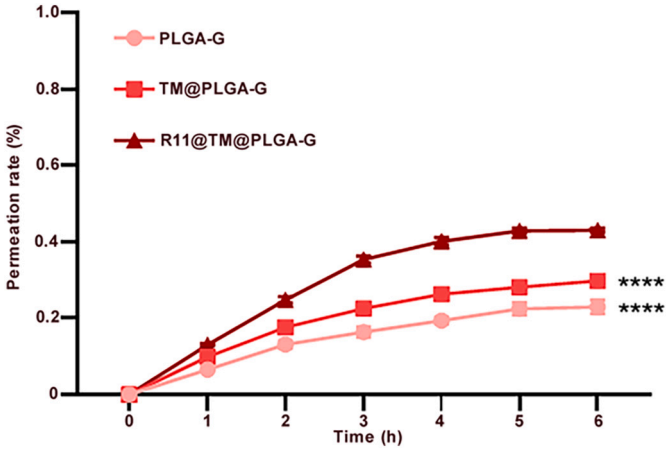

Fig. 3. GAG layer permeation assay. For convenience of quantification, Gem was replaced with coumarin-6; **** $p < 0.0001$.

3.2. Penetration efficiency through the GAG layer

The inner layer of the bladder lumen is composed of highly specialized umbrella cells. The surface of the umbrella cell membrane is covered with a special membrane consisting of urokinase, lectin and GAG layers [26–28]. Chondroitin sulfate is the major component in the GAG layer, which is located on the luminal surface of the urothelium and provides the greatest contribution to the urothelial protective barrier function [25]. By loading chondroitin sulfate into the upper chamber of the Transwell plate to mimic the GAG layer, the permeation rates of cargos loaded in PLGA-G, TM@PLGA-G and R11@TM@PLGA-G through the GAG layer were calculated to be 23.0 ± 1.4%, 29.8 ± 0.5%, and 43.1 ± 0.4%, respectively (Fig. 3). Surface functionalization with R11 improved the penetration efficiency of cargos inside the TM through the GAG layer ($P < 0.0001$).

3.3. Targeting efficiency, internalization behavior, and intracellular trafficking fate

As shown in Fig. 4A-C, the fluorescence intensities of T24, T24l and 253 J 5.5 ± 0.8, 4.0 ± 0.3 and 4.1 ± 0.7 times that of normal urothelial

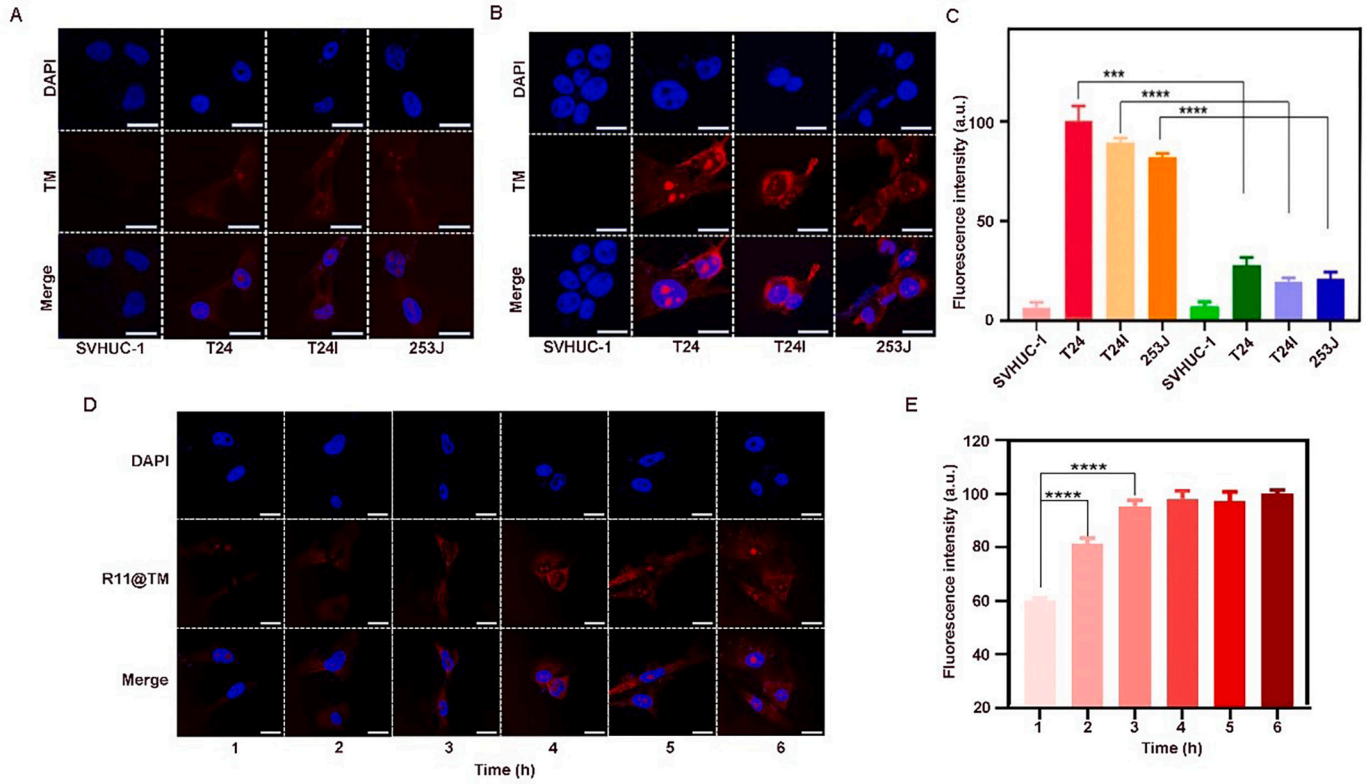

Fig. 4. The BCa targeting efficiency and the endocytosis dynamics. A) CLSM analysis of the BCa Targeting Efficiency of TM; scale bar: 25 μm. B) CLSM analysis of the BCa Targeting Efficiency of R11@TM; scale bar: 25 μm. C) Statistical analysis of the BCa Targeting Efficiency of R11@TM; **** $p < 0.0001$. D) CLSM analysis of the endocytosis dynamics of R11@TM; scale bar: 25 μm. E) Statistical analysis of the endocytosis dynamics of R11@TM. **** $p < 0.0001$.

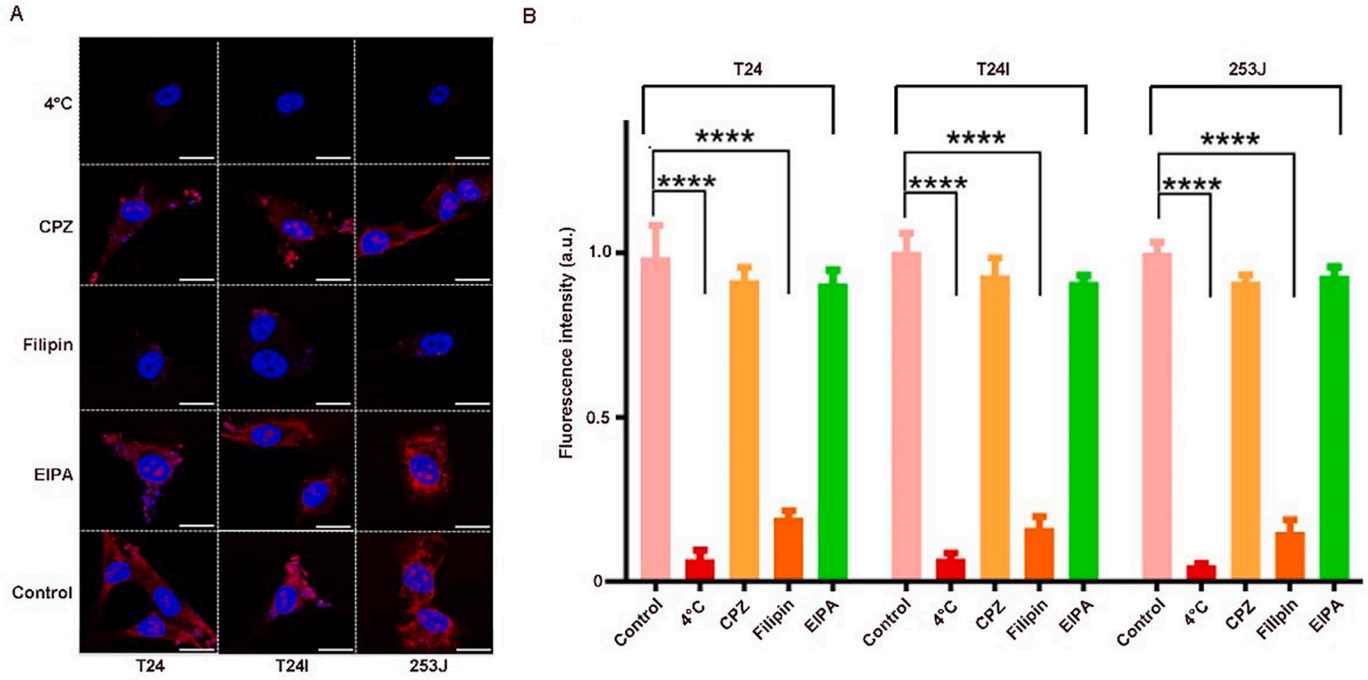

Fig. 5. The endocytosis pathway of R11@TM. A) CLSM analysis of the endocytosis inhibition by different treatments; Scar bar: 25 μm. B) Statistical analysis of the endocytosis inhibition by different treatments; **** $p < 0.0001$.

cells (SVHUC-1) in the TM group, respectively. The fluorescence intensities of T24, T24l and 253 J were quantified to be approximately 13 times that of SVHUC-1 in the R11@TM group. The surface functionalization with R11 endowed TM with the dual-targeting capacity, which originated from the intrinsic BCa targeting capacity of R11 [21] and the homologous tumor targeting capacity of TM. At regular

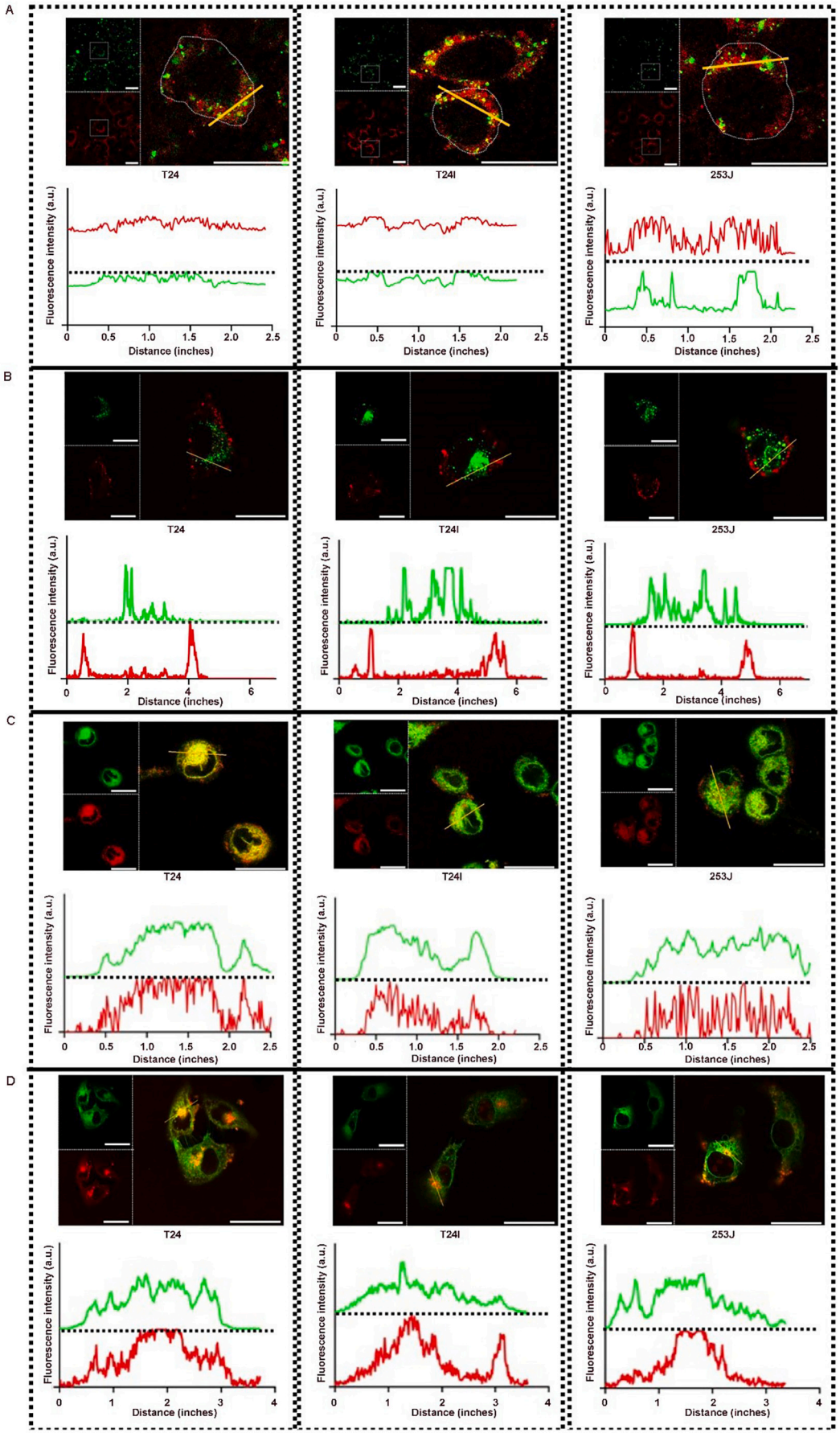

(caption on next page)

Fig. 6. The intracellular trafficking fate of R11@TM. A) The intracellular colocalization of dual components of R11@TM; Red: R11; Green: TM; Scar bar: 25 μm for small images, 25 μm for enlarged images. B) The subcellular colocalization of R11@TM and lysosomes; Red: R11@TM; Green: lysotracker; Scar bar: 25 μm for small images, 25 μm for enlarged images. C) The subcellular colocalization of R11@TM and the ER; Red: R11@TM; Green: ER tracker; Scar bar: 25 μm for small images,25 μm for enlarged images. D) The subcellular colocalization of R11@TM and the the Golgi apparatus; Red: R11@TM; Green: Golgi tracker; Scar bar: 25 μm for small images, 25 μm for enlarged images. (For interpretation of the references to colour in this figure legend, the reader is referred to the web version of this article.)

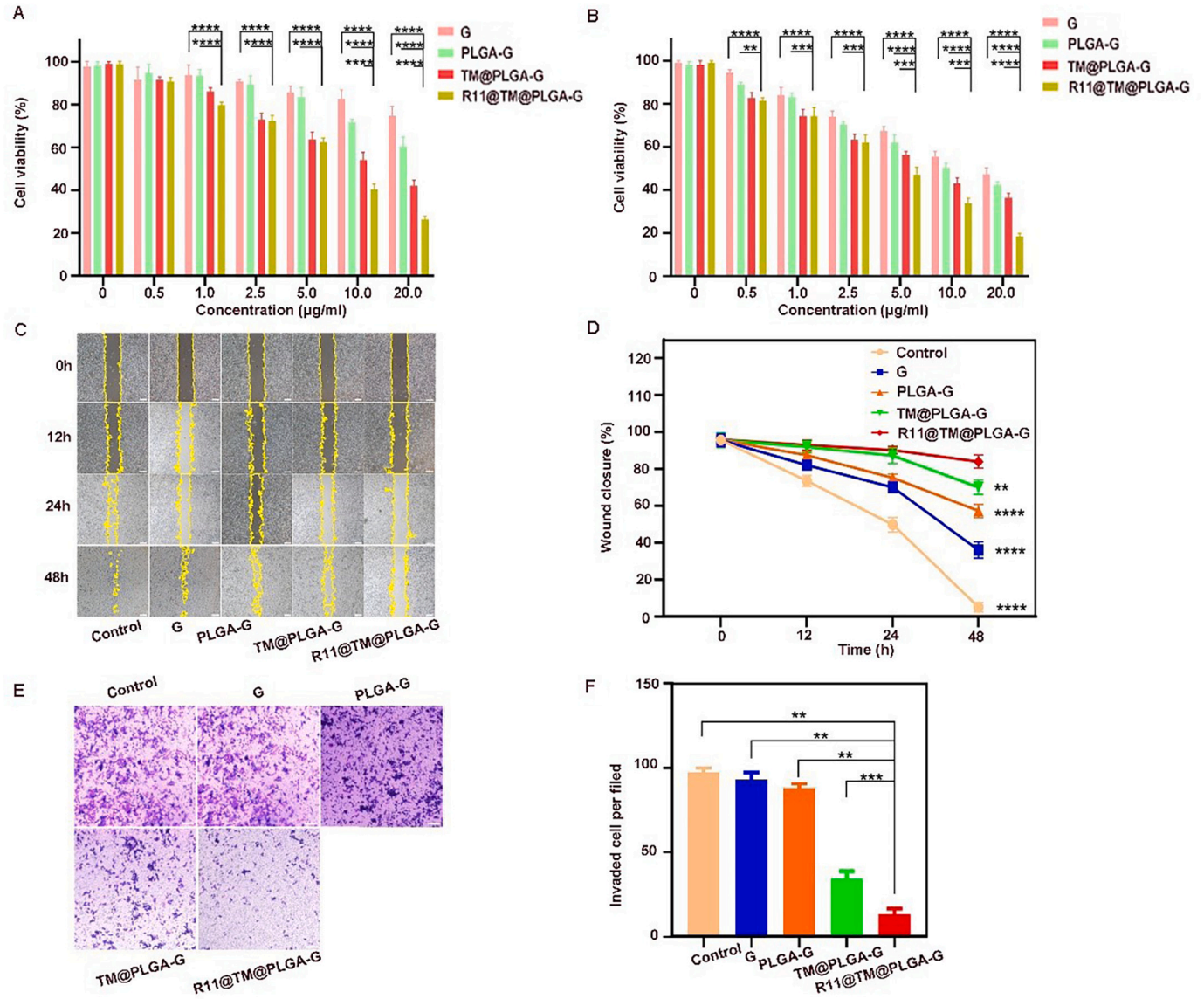

Fig. 7. Anti-tumor effect *in vitro*. A) Cytotoxicity of different treatments for 24 h incubation; **** $p < 0.0001$. B) Cytotoxicity of different treatments for 48 h incubation; ** $p < 0.01$, *** $p < 0.001$, **** $p < 0.0001$. C) Effect of different treatments on T24 cell migration as determined by scratch wound healing assay; scale bar: 200 μm. D) Statistical analysis of the effect of different treatments on T24 cell migration as determined by scratch wound healing assay; ** $p < 0.01$, **** $p < 0.0001$. E) Effect of different treatments on T24 cell invasion as detected by Transwell assay; scale bar: 200 μm. F) Statistical analysis of the effect of different treatments on T24 cell invasion as detected by Transwell assay; ** $p < 0.01$, *** $p < 0.001$.

intervals of one hour, the endocytosis dynamics of R11@TM in T24 cells were also studied (Fig. 4D-E). At a coincubation time of 3 h, the average fluorescence per cell reached the peak intensity. The endocytosis mechanism was further studied. CPZ, filipin and EIPA were used to block the clathrin-mediated endocytosis pathway, the caveolin-mediated pathway, and macropinocytosis, respectively [29,30]. A temperature of 4 °C was also used to block energy-dependent endocytosis [31]. The endocytosis of R11@TM was significantly inhibited by 4 °C or filipin in T24, T24l and 253 J cells (Fig. 5A-B). It has been recognized that endocytosis through the caveolin-mediated pathway determines the intracellular trafficking of nanoparticles to nonlysosome-localized regions [32]. One issue of concern was the intracellular disassembly of R11 from R11@TM. The cytoplasm is a pool that contains a large number of negatively charged molecules, which might interact with positively charged R11. As displayed in Fig. 6A, the spatial correlation of the two components was strong for endocytic R11@TM to some extent, although part of R11 was exfoliated from R11@TM. The subcellular localization of R11@TM was confined to the ER and Golgi apparatus rather than lysosomes in T24, T24L and 253 J cells (Fig. 6B-D). Therefore, the drugs loaded in R11@TM were capable of escaping the fate of degradation in lysosomes [33].

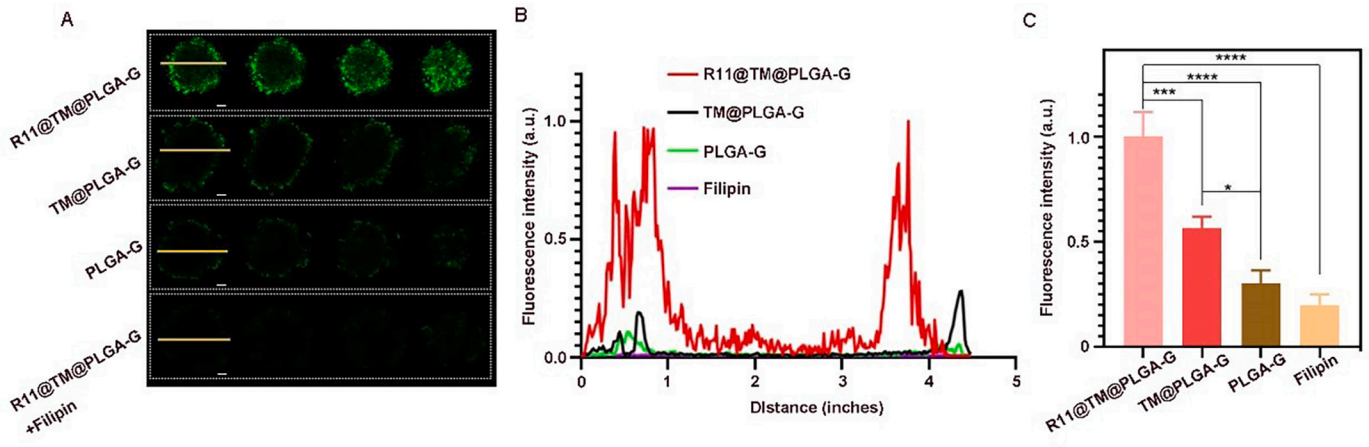

Fig. 8. Penetration efficiency in tumor spheroids. A) CLSM analysis of the penetration efficiency of coumarin-6 in R11@TM@PLGA-coumarin-6 group, TM@PLGA-coumarin-6 group, PLGA-coumarin-6 group and filipin-pretreated R11@TM@PLGA-coumarin-6 group; Scar bar: 100 μm. B) The fluorescence distribution of PLGA-coumarin-6 inside tumor spheroids in different-treatment groups; The fluorescence intensity was obtained along the yellow line in (a). C) Statistical analysis of the average fluorescence intensity of PLGA-coumarin-6 accumulated inside tumor spheroids in different-treatment groups; ** $p < 0.01$, **** $p < 0.001$. (For interpretation of the references to colour in this figure legend, the reader is referred to the web version of this article.)

3.4. Antitumor effect in vitro

The inhibitory effects of G, PLGA-G, TM@PLGA-G and R11@TM@PLGA-G on the proliferation of T24 cells were studied. Time-dependent and concentration-dependent cytotoxicity could be observed for all forms of G, among which R11@TM@PLGA-G showed the best antitumor effect on T24 cells (Fig. 7A-B). whereas R11@TM@PLGA-G, rather than other forms of G, nearly exposed no cytotoxicity to normal urothelial cells (Fig. S4). Consistent with previous studies [34], R11@TM@PLGA-G induced an S phase accumulation to the most extent (**Fig. S5A**). The migration and invasion abilities were most severely attenuated by R11@TM@PLGA-G treatment (Fig. 7C-F), and Western blotting analysis revealed that its inhibition on epithelial-mesenchymal transition (EMT) might be the mechanism [35,36]. With a non-cytotoxic concentration, E-cadherin, ZO-1 and Claudin were up-regulated, while N-cadherin was down-regulated (**Fig. S5B**). Together, EMT-inhibition and S-phase blocking might contribute to the anti-tumor effect of R11@TM@PLGA-G.

3.5. Penetration efficiency in tumor spheroids

Multicellular spheroids (MCSs) have been proposed as an *in vitro* 3D-cultured tumor model to evaluate the tumor penetration of drugs [34]. In this study, T24 MCSs were established to study the penetration efficiency. G was replaced with coumarin-6 to fluorescently label PLGA-G, TM@PLGA-G and R11@TM@PLGA-G. As presented in Fig. 8A-C, the infiltration depth of coumarin-6 was limited to the outer regions of T24 MCSs in the PLGA-G group and in the TM@PLGA-G group, whereas coumarin-6 could migrate into the inner regions of T24 MCSs in the R11@TM@PLGA-G group. In accordance with endocytosis inhibition by filipin in 2D cell culture models, filipin also hampered the penetrating ability of coumarin-6 in the R11@TM@PLGA-G group.

3.6. Antitumor effect in murine orthotopic BCa models

The murine orthotopic BCa model was an excellent option for testing the *in vivo* targeting and penetration efficiency of intravesically instilled drugs [37–40]. The targeting and penetration efficacies of most drugs remained far below expectations during the short instillation time [41]. Surface functionalization of TM@PLGA-G with R11 enabled TM@PLGA-G to specifically accumulate in tumor regions, as presented in Fig. 9A. R11@TM@PLGA-G could penetrate the inner regions of tumors rather than remain in the outer regions (Fig. 9B). The antitumor effect was also compared between saline, G, PLGA-G, TM@PLGA-G and R11@TM@PLGA-G in murine orthotopic BCa models. R11@TM@PLGA-G exhibited the best antitumor effect, reflected by the fact that it could even chemoresect tumors in three of five cases with no recurrence for the remaining days. The antitumor effects of TM@PLGA-G, PLGA-G, and G ranked second, third and fourth, respectively (Fig. 9C). Normal organs, including the heart, liver, spleen, lung and kidney, were transferred for pathological examination by hematoxylin eosin (HE) staining. No obvious pathological change could be detected (Fig. 9D). The average weight steadily increased for the groups in which tumor progression was delayed, and it decreased after entering the metaphase of intravesical therapy for the groups in which tumor progression proceeded (Fig. 9E). Therefore, R11@TM@PLGA-G exhibits potential for intravesical therapy of BCa due to its therapeutic effectiveness and biosafety.

4. Conclusions

Intravesical therapy for BCa is limited in efficacy due to the permeation barrier and side effects caused by the off-targeting of normal urothelial cells. In this study, we demonstrated a simple surface functionalization method to construct dual-targeting and mucus-penetrating cell membrane nanovesicles for delivering chemotherapeutic drugs through intravesical instillation. Because of the simplicity of synthesis, the antitumor effect and the biosafety, the dual-targeting and mucus-penetrating drug delivery system has promising potential for further clinical use.

Availability of data and materials

All data generated or analyzed during this study are included in this published article and its supplementary information files.

Credit author statement

Bin Zheng is responsible for the data curation, investigation, writing - original draft. Zhenghong Liu and Heng Wang did the data curation, and writing - original draft. Li Sun, Wing-Fu Lai and Haibao Zhang did the software. Jinxue Wang, Yang Liu and Xiaowen Qin writing - review. Xiaolong Qi is responsible for formal analysis and editing. Shuai Wang did the validation. Youqing Shen, Pu Zhang and Dahong Zhang is responsible for the conceptualization, methodology, funding acquisition, supervision. All authors read and approved the final manuscript.

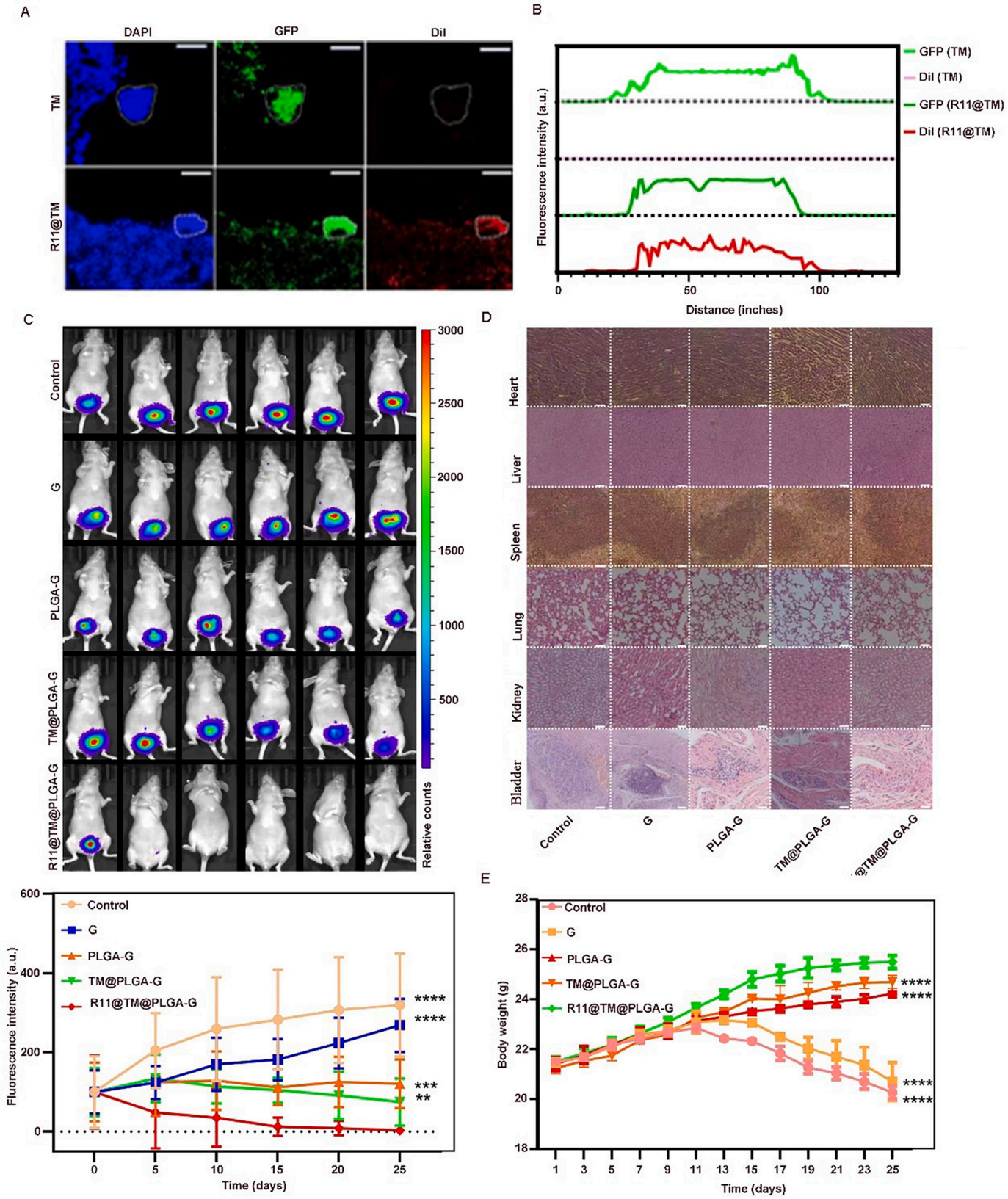

Fig. 9. Anti-tumor effect in murine orthotopic BCa models. A) The colocalization of DiI-labeled different nanovesicles and GFP-labeled tumor regions after a single intravesical instillation in murine orthotopic BCa models; scar bar: 100 μm. B) The fluorescence distribution of DiI-labeled different nanovesicles inside GFP-labeled tumor regions; Dotted line: fluorescence baseline. C) Anti-tumor activity against orthotopic T24-Luci BCa illustrated by *in vivo* bioluminescence images (up) and *in vivo* bioluminescence images intensity (down); ** $p < 0.01$,*** $p < 0.001$, **** $p < 0.0001$. D) Histopathological analysis of normal organs and bladders harvested from different-treatment groups; Scar bar: 200 μm. E) Average weight during the intravesical therapy; **** $p < 0.0001$.

Declaration of Competing Interest

The authors declare no conflicts of interest in this work.

Data availability

Data will be made available on request.

Acknowledgements

This research was funded by Medical Technology Plan of Zhejiang Province (grant number: 2021421701), Medical Technology Plan of Zhejiang Province (grant number: 2022497314), the Natural Science Foundation of Zhejiang Province (grant number: LQ21H160041), the Natural Science Foundation of Zhejiang Province (grant number: LBQ20H050001). T24l was provided by Professor Jinhai Fan (Xi'an Jiaotong University).

Appendix A. Supplementary data

Supplementary data to this article can be found online at https://doi.org/10.1016/j.jconrel.2022.09.055.

References

[1] T. Kobayashi, T.B. Owczarek, J.M. McKiernan, C. Abate-Shen, Modelling bladder cancer in mice: opportunities and challenges, Nat. Rev. Cancer 15 (2015) 42–54, https://doi.org/10.1038/nrc3858.
[2] S. Antoni, J. Ferlay, I. Soerjomataram, A. Znaor, A. Jemal, F. Bray, Bladder cancer incidence and mortality: a global overview and recent trends, Eur. Urol. 71 (2017) 96–108, https://doi.org/10.1016/j.eururo.2016.06.010.
[3] R.M. Davis, B. Kiss, D.R. Trivedi, T.J. Metzner, J.C. Liao, S.S. Gambhir, Surface-enhanced Raman scattering nanoparticles for multiplexed imaging of bladder Cancer tissue permeability and molecular phenotype, ACS Nano 12 (2018) 9669–9679, https://doi.org/10.1021/acsnano.8b03217.
[4] L. Neutsch, B. Eggenreich, E. Herwig, M. Marchetti-Deschmann, G. Allmaier, F. Gabor, M. Wirth, Lectin bioconjugates trigger urothelial cytoinvasion–a glycotargeted approach for improved intravesical drug delivery, Eur. J. Pharm. Biopharm. 82 (2012) 367–375, https://doi.org/10.1016/j.ejpb.2012.07.016.
[5] S. GuhaSarkar, R. Banerjee, Intravesical drug delivery: challenges, current status, opportunities and novel strategies, J. Control. Release 148 (2010) 147–159, https://doi.org/10.1016/j.jconrel.2010.08.031.
[6] M. Babjuk, A. Böhle, M. Burger, O. Capoun, D. Cohen, E.M. Compérat, V. Hernández, E. Kaasinen, J. Palou, M. Rouprêt, B.W.G. van Rhijn, S.F. Shariat V. Soukup, R.J. Sylvester, R. Zigeuner, EAU guidelines on non-muscle-invasive urothelial carcinoma of the bladder: update 2016, Eur. Urol. 71 (2017) 447–461, https://doi.org/10.1016/j.eururo.2016.05.041.
[7] S.S. Chang, S.A. Boorjian, R. Chou, P.E. Clark, S. Daneshmand, B.R. Konety, R. Pruthi, D.Z. Quale, C.R. Ritch, J.D. Seigne, E.C. Skinner, N.D. Smith, J. M. McKiernanet, Diagnosis and treatment of non-muscle invasive bladder cancer: AUA.SUO guideline, J. Urol. 196 (2016) 1021–1029, https://doi.org/10.1016/j.juro.2016.06.049.
[8] N. Kong, R. Zhang, G. Wu, X. Sui, J. Wang, N.Y. Kim, S. Blake, D. De, T. Xie, Y. Cao, W. Tao, KDM6AIntravesical delivery of -mRNA via mucoadhesive nanoparticles inhibits the metastasis of bladder cancer, P. Natl. Acad. Sci. 119 (2022) 1–12, https://doi.org/10.1073/pnas.2112696119.
[9] P. Tyagi, P.C. Wu, M. Chancellor, N. Yoshimura, L. Huang, Recent advances in intravesical drug/gene delivery, Mol. Pharm. 3 (2006) 369–379, https://doi.org/10.1021/mp060001j.
[10] C. Apfelthaler, M. Anzengruber, F. Gabor, M. Wirth, Poly - (l) - glutamic acid drug delivery system for the intravesical therapy of bladder cancer using WGA as targeting moiety, Eur. J. Pharm. Biopharm. 115 (2017) 131–139, https://doi.org/10.1016/j.ejpb.2017.02.016.
[11] S.A. Lewis, Everything you wanted to know about the bladder epithelium but were afraid to ask, Am. J. Physiol. Ren. Physiol. 278 (2000) 867–874, https://doi.org/10.1152/ajprenal.2000.278.6.F867.
[12] A. Giannantoni, S.M. Di Stasi, M.B. Chancellor, E. Costantini, New frontiers in intravesical therapies and drug delivery, Eur. Urol. 50 (2006) 1183–1193, https://doi.org/10.1016/j.eururo.2006.08.025.
[13] S.M. Di Stasi, A. Giannantoni, A. Giurioli, M. Valenti, G. Zampa, L. Storti, F. Attisani, A. De Carolis, G. Capelli, G. Vespasiani, R.L. Stephen, Sequential BCG and electromotive mitomycin versus BCG alone for high-risk superficial bladder cancer: a randomised controlled trial, Lancet Oncol. 7 (2006) 43–51, https://doi.org/10.1016/S1470-2045(05)70472-1.
[14] M.O. Fraser, Y.C. Chuang, P. Tyagi, T. Yokoyama, N. Yoshimura, L. Huang, W.C. De Groat, M.B. Chancellor, Intravesical liposome administration–a novel treatment for hyperactive bladder in the rat, Urology 61 (2003) 656–663, https://doi.org/10.1016/s0090-4295(02)02281-1.
[15] L.C. Chang, S.C. Wu, J.W. Tsai, T.J. Yu, T.R. Tsai, Optimization of epirubicin nanoparticles using experimental design for enhanced intravesical drug delivery, Int. J. Pharm. 376 (2009) 195–203, https://doi.org/10.1016/j.ijpharm.2009.04.045.
[16] M. Kerec, M. Bogataj, P. Veranic, A. Mrhar, Permeability of pig urinary bladder wall: the effect of chitosan and the role of calcium, Eur. J. Pharm. Biopharm. 25 (2005) 113–121, https://doi.org/10.1016/j.ejps.2005.02.003.
[17] T. Leakakos, C. Ji, G. Lawson, C. Peterson, S. Goodwin, Intravesical administration of doxorubicin to swine bladder using magnetically targeted carriers, Cancer Chemother. Pharmacol. 51 (2003) 445–450, https://doi.org/10.1007/s00280-003-0597-9.
[18] H. Zhou, Z. Fan, P.K. Lemons, H. Cheng, A facile approach to functionalize cell membrane-coated nanoparticles, Theranostics. 6 (2016) 1012–1022, https://doi.org/10.7150/thno.15095.
[19] Z. Chen, P. Zhao, Z. Luo, M. Zheng, H. Tian, P. Gong, G. Gao, H. Pan, L. Liu, A. Ma, H. Cui, Y. Ma, L. Cai, Cancer cell membrane-biomimetic nanoparticles for homologous-targeting dual-modal imaging and Photothermal therapy, ACS Nano 10 (2016) 10049–10057, https://doi.org/10.1021/acsnano.6b04695.
[20] M. Zhang, S. Cheng, Y. Jin, N. Zhang, Y. Wang, Membrane engineering of cell membrane biomimetic nanoparticles for nanoscale therapeutics, Clin. Transl. Med. 11 (2021) 292–303, https://doi.org/10.1002/ctm2.292.
[21] Y. Du, L. Wang, W. Wang, T. Guo, M. Zhang, P. Zhang, Y. Zhang, K. Wu, A. Li, X. Wang, J. He, J. Fan, Novel application of cell penetrating R11 peptide for diagnosis of bladder Cancer, J. Biomed. Nanotechnol. 14 (2018) 161–167, https://doi.org/10.1166/jbn.2018.2499.
[22] A. Mann, R. Richa, M. Ganguli, DNA condensation by poly-L-lysine at the single molecule level: role of DNA concentration and polymer length, J. Control. Release 125 (2008) 252–262, https://doi.org/10.1016/j.jconrel.2007.10.019.
[23] Z. Zhang, D. Li, X. Li, Z. Guo, Y. Liu, X. Ma, S. Zheng, PEI-modified macrophage cell membrane-coated PLGA nanoparticles encapsulating Dendrobium polysaccharides as a vaccine delivery system for ovalbumin to improve immune responses, Int. J. Biol. Macromol. 165 (2020) 239–248, https://doi.org/10.1016/j.ijbiomac.2020.09.187.
[24] R.H. Fang, A.V. Kroll, W. Gao, L. Zhang, Cell membrane coating nanotechnology, Adv. Mater. 30 (2018) 1706759–1706768, https://doi.org/10.1002/adma.201706759.
[25] S. Behzadi, C. Rosenauer, K. Kappl, K. Mohr, K. Landfester, D. Crespy, Osmotic pressure-dependent release profiles of payloads from nanocontainers by co-encapsulation of simple salts, Nanoscale 8 (2016) 12998–13005, https://doi.org/10.1039/c6nr01882c.
[26] S. Hamamoto, T. Takemura, K. Suzuki, T. Nishimura, Effects of pH on nano-bubble stability and transport in saturated porous media, J. Contam. Hydrol. 208 (2018) 61–67, https://doi.org/10.1016/j.jconhyd.2017.12.001.
[27] M. Buckley, P. Xin, S. Washington, N. Herb, D. Erickson, V.P. Bhavanandan, Lectin histochemical examination of rabbit bladder glycoproteins and characterization of a mucin isolated from the bladder mucosa, Arch. Biochem.Biophys. 375 (2000) 270–277, https://doi.org/10.1006/abbi.1999.1664.
[28] R.E. Hurst, J.B. Roy, K.W. Min, R.W. Veltri, G. Marley, K. Patton, D.L. Shackelford, P. Stein, C.L. Parsons, A deficit of chondroitin sulfate proteoglycans on the bladder uroepithelium in interstitial cystitis, Urology 48 (1996) 817–821, https://doi.org/10.1016/S0090-4295(96)00322-6.
[29] D. Yılmaz, M. Culha, Investigation of the pathway dependent endocytosis of gold nanoparticles by surface-enhanced Raman scattering, Talanta 225 (2021) 122071–122080, https://doi.org/10.1016/j.talanta.2020.122071.
[30] Y. Caì, E.N. Postnikova, J.G. Bernbaum, S.Q. Yú, S. Mazur, N.M. Deiuliis, S. R. Radoshitzky, M.G. Lackemeyer, A. McCluske, P.J. Robinson, V. Haucke, V. Wahl-Jensen, A.L. Bailey, M. Lauck, T.C. Friedrich, D.H. O'Connor, T. L. Goldberg, P.B. Jahrling, J.H. Kuhn, Simian hemorrhagic fever virus cell entry is dependent on CD163 and uses a clathrin-mediated endocytosis-like pathway, J. Virol. 89 (2015) 844–856, https://doi.org/10.1128/JVI.02697-14.
[31] N. Nagai, F. Ogata, H. Otake, Y. Nakazawa, N. Kawasaki, Energy-dependent endocytosis is responsible for drug transcorneal penetration following the instillation of ophthalmic formulations containing indomethacin nanoparticles, Int. J. Nanomedicine 14 (2019) 1213–1227, https://doi.org/10.2147/IJN.S196681.
[32] S. Chen, Y. Zhong, W. Fan, J. Xiang, G. Wang, Q. Zhou, J. Wang, Y. Geng, R. Sun, Z. Zhang, Y. Piao, J. Wang, J. Zhuo, H. Cong, H. Jiang, J. Ling, Z. Li, D. Yang, X. Yao, X. Xu, Z. Zhou, J. Tang, Y. Shen, Enhanced tumour penetration and prolonged circulation in blood of polyzwitterion-drug conjugates with cell-membrane affinity, Nat. Biomed. Eng. 5 (2021) 1019–1037, https://doi.org/10.1038/s41551-021-00701-4.
[33] C.G. Liu, Y.H. Han, R.K. Kankala, S.B. Wang, A.Z. Chen, Subcellular performance of nanoparticles in Cancer therapy, Int. J. Nanomedicine 15 (2020) 675–704, https://doi.org/10.2147/IJN.S226186.
[34] A.D. Adema, A.C. Laan, F. Myhren, I. Fichtner, H.M. Verheul, M.L. Sandvold, G. J. Peters, M. Isono, K. Okubo, T. Asano, A. Sato, Inhibition of checkpoint kinase 1 potentiates anticancer activity of gemcitabine in bladder cancer cells, Sci. Rep-UK. 11 (2021) 10181–10188, https://doi.org/10.1038/s41598-021-89684-5.
[35] S.S. Islam, R.B. Mokhtari, A.S. Noman, M. Uddin, M.Z. Rahman, M.A. Azadi, A. Zlotta, T. van der Kwast, H. Yeger, W.A. Farhat, Sonic hedgehog (Shh) signaling promotes tumorigenicity and stemness via activation of epithelial-to-mesenchymal transition (EMT) in bladder cancer, Mol. Carcinog. 55 (2016) 537–551, https://doi.org/10.1002/mc.22300.
[36] A. Li, X. Zhu, C. Wang, S. Yang, Y. Qiao, R. Qiao, J. Zhang, Upregulation of NDRG1 predicts poor outcome and facilitates disease progression by influencing the EMT process in bladder cancer, Sci. Rep-UK. 9 (2019) 5166–5176, https://doi.org/10.1038/s41598-019-41660-w.

[37] Q. Zhou, S. Shao, J. Wang, C. Xu, J. Xiang, Y. Piao, Z. Zhou, Q. Yu, J. Tang, X. Liu, Z. Gan, R. Mo, Z. Gu, Y. Shen, Enzyme-activatable polymer-drug conjugate augments tumour penetration and treatment efficacy, Nat. Nanotechnol. 14 (2019) 799–809, https://doi.org/10.1038/s41565-019-0485-z.

[38] H. Doreen, R. Christiane, B. Ralf, U. Martin, M. Sebastian, T. Marieta, W. Ralf, T. Achim, N. Vladimir, P. Manfred, B. Michael, P. Jens, F. Susanne, An orthotopic xenograft model for high-risk non-muscle invasive bladder cancer in mice: influence of mouse strain, tumor cell count, dwell time and bladder pretreatment, BMC Cancer 17 (2017) 790–802, https://doi.org/10.1186/s12885-017-3778-3.

[39] M. Roelants, B. Van Cleynenbreugel, H. Van Poppel, E. Lerut, P.A. de Witte, Use of fluorescein isothiocyanate-human serum albumin for the intravesical photodiagnosis of non-muscle-invasive bladder cancer: an in vitro study using multicellular spheroids composed of normal human urothelial and urothelial cell carcinoma cell lines, BJU Int. 108 (2011) 455–459, https://doi.org/10.1111/j.1464-410X.2010.09951.x.

[40] I. Vasyutin, L. Zerihun, C. Ivan, A. Atala, Bladder organoids and spheroids: potential tools for Normal and diseased tissue modelling, Anticancer Res. 39 (2019) 1105–1118, https://doi.org/10.21873/anticanres.13219.

[41] Y. Abidine, A. Giannetti, J. Revilloud, V.M. Lauren, C. Verdier, Viscoelastic properties in Cancer: from cells to spheroids, Cells Basel 10 (2021) 1–15, https://doi.org/10.3390/cells10071704.